

Effect of Creep on Corrosion-Induced Cracking

Ismail Aldellaa¹, Petr Havlásek², Milan Jirásek², Peter Grassl^{1*}

¹James Watt School of Engineering, University of Glasgow, Glasgow, UK

²Czech Technical University in Prague, Czechia

*Corresponding author: Email: peter.grassl@glasgow.ac.uk

Abstract

Corrosion-induced cracking is the most widely encountered and studied long-term deterioration process in reinforced concrete. Naturally occurring corrosion rates are so low that rust accumulates often over tens of years near the surface of the reinforcement bars before sufficient pressure in the surrounding concrete is generated to induce cracking in the concrete cover. To speed up the process in laboratory tests, corrosion setups with impressed currents have been developed in which the corrosion rate is controlled to be so high that cracking of the concrete cover occurs within a few days. Extrapolating the results of these accelerated tests to those of naturally occurring corrosion requires an understanding of the influence of long-term creep deformations of concrete on the corrosion-induced cracking process. In mathematical models in the literature, creep deformations are often ignored for accelerated but considered for natural corrosion rates in the form of an effective modulus.

In this work, three numerical models of increasing complexity are proposed with the aim to investigate the effect of creep on corrosion-induced cracking. The simplest approach is based on an uncracked axis-symmetric thick-walled cylinder combined with a plastic limit on the radial pressure-induced by the accumulation of rust. The model with intermediate complexity comprises a thick-walled cylinder model divided into an inner cracked and an outer uncracked layer. The most comprehensive model consists of a thick-walled cylinder discretised by a three-dimensional lattice approach. Basic creep is predicted in all three approaches by means of the B3 model developed by Bažant and co-workers. Time dependence of strength of concrete is modelled using *fib* Model Code expressions. It is shown that for the comprehensive lattice model, creep has limited influence on critical corrosion penetration, which indicates that the dependence of the critical corrosion penetration on corrosion rate must have other sources.

1 Introduction

The most commonly encountered deterioration process of steel reinforced concrete is corrosion-induced cracking (Broomfield, 1997). Cracking occurs due to the formation of an expansive layer of

corrosion products which is located close to the interface between concrete and reinforcement. Predictive models for corrosion-induced cracking are here divided into three groups, namely uncracked axis-symmetric thick-walled cylinder models, cracked axis-symmetric thick-walled cylinder models and lattice models. All these models are mechanistic instead of imperial or semi-imperial.

The first two groups are based on the mechanics of an axis-symmetric thick-walled cylinder. These models are popular because the solution can be obtained quickly by solving an ordinary differential equation, without the need for spatial discretisation. Many articles have investigated the performance of these models, which are reviewed in Jamali et al. (2013), Roshan et al. (2020) and Liang and Wang (2020). Uncracked axis-symmetric thick-walled cylinder models construct a plastic limit on the radial pressure at the inner boundary. Examples of these uncracked cylinder models are Bažant (1979b) and Liu and Weyers (1998). One of the well known shortcomings of this original approach is that the time to surface cracking is underestimated because the effect of material nonlinearities on the compliance of the cylinder are not taken into consideration. The overestimated stiffness leads to an underestimated displacement at the inner boundary at the time when the limit state is reached. This deficiency is alleviated by a newly proposed modification that takes into account the plastic strains and corrects the resulting compliance, described in Section 2.1.2.

Cracked cylinder models still use the assumption of the axis-symmetric thick-walled cylinder, but divide the cylinder into an inner cracked and an outer uncracked layer, with the division progressing to the outer boundary during the corrosion process. The original idea of the two layers was proposed for bond between concrete and reinforcement in Tepfers (1979) and then adapted for corrosion-induced cracking in Pantazopoulou and Papoulia (2001). Further modifications of these models were made in Li et al. (2006), Bhargav et al. (2006) and Chernin et al. (2010). These models have the advantage that they can describe the material nonlinearities and, therefore, predict the stiffness of the thick-walled cylinder correctly. The nonlinearity is introduced by transforming the opening of an assumed number of cracks into an axis-symmetric cracking strain. Once the cracked cylinder reaches the outer boundary, the assumption of axis-symmetry is not valid anymore and these thick-walled cylinder models cease to produce reliable results.

The lattice approaches are based on the spatial discretisation of the specimen using discrete elements within a matrix analysis approach. Many of the limitations of the thick-walled cylinder models are overcome by means of the spatial discretisation. No assumptions are required on the number of cracks. Furthermore, crack propagation beyond the occurrence of a surface crack can be modelled. However, approaches based on spatial discretisation are computationally much more time intensive and require techniques to model crack formation independent of the discretisation. Many of these lattice approaches have been successfully used to model cracks in concrete at the meso-scale (Schlangen and van Mier, 1992; Montero-Chacón et al., 2017; Chang et al., 2020; Thilakarathna et al., 2020) and macro-scale (Bolander and Saito, 1998; Asahina et al., 2017). Lattice models can incorporate constitutive models, formulated in terms of tractions and displacement jumps, as commonly used in interface approaches for concrete fracture (Caballero et al., 2006; Zhou and Lu, 2018). An example of this is the damage plasticity lattice model used in Grassl and Davies (2011) and Athanasiadis et al. (2018), which is used in this study. As shown in Grassl and Jirásek (2010), these models yield element size-independent descriptions of crack openings provided that fracture is localised. For initially distributed cracking such as for the case of corrosion-induced cracking, potential mesh dependence can be strongly reduced by introducing random fields of ma-

terial strength as done by Grassl and Jirásek (2010). This approach is adopted here as well. For the lattice approach used in this study, the spatial arrangement of the lattice elements and their cross-sectional properties are based on Delaunay and Voronoi tessellations of a set of random points placed in the domain as developed in Yip et al. (2005). The random placement of nodes reduces the influence of the discretisation on the fracture patterns, as observed for other fracture approaches (Grassl and Rempling, 2007; Jirásek and Grassl, 2008).

All the above approaches have in common that loading is applied by the formation of an expansive layer of corrosion products at the steel-concrete interface. These products are formed by corrosion, which is an electro-chemical process driven by the corrosion current density, normally so small that cracking is obtained only after many years (Broomfield, 1997). To accelerate the process in laboratory tests, an impressed current is applied, which increases the corrosion rate so that cracking can be obtained within days instead of years (Andrade et al., 1993). To be able to use the results of these tests for predictive modelling of corrosion-induced cracking, it is required to relate the accelerated results to those of naturally occurring corrosion. Experimental studies have investigated various aspects in which naturally occurring corrosion-induced cracking differs from accelerated tests using currents. For instance, corrosion products resulting from naturally occurring corrosion are not uniformly distributed around the steel bar circumference, but are more prominent in locations that are exposed to more severe conditions (e.g., direction of carbonation front and gradient of ingress of chlorides) (Zhao et al., 2011). Furthermore, corrosion products forming in the vicinity of the steel-concrete interface are found to migrate into pores and cracks (Wong et al., 2010; Michel et al., 2014; Robuschi et al., 2021), which affects the build up of pressure and is often considered in modelling approaches (Liu and Weyers, 1998; Chernin et al., 2010). In addition, compaction of corrosion products has been investigated experimentally in Ouglova et al. (2006) and incorporated in several modelling approaches (Lundgren, 2005; Balafas and Burgoyne, 2011). The composition of the corrosion products differs in naturally occurring corrosion from accelerated tests (El Maaddawy and Soudki, 2003). Therefore, it is expected that the influence of migration and compaction of corrosion products will differ in natural and accelerated corrosion tests.

Long-term effects of the surrounding concrete is another phenomenon which has not been studied extensively in the context of corrosion-induced cracking. When concrete is subjected to sustained load, it exhibits creep deformations that grow in time. Furthermore, strength and stiffness of concrete increase with age. This time-dependent response of concrete has been well studied in the literature (L'Hermite et al., 1965; Kommendant et al., 1976; Bryant and Vadhanavikkit, 1987; Bažant and Jirásek, 2018). However, its effect on corrosion-induced cracking has not been investigated in detail yet. In the literature, corrosion-induced cracking models based on axis-symmetric thick-walled cylinder models often approximate the effect of creep for naturally occurring corrosion by replacing the short-term Young modulus with an effective modulus that is reduced by a creep coefficient. For accelerated corrosion, creep has often been disregarded, with the argument that cracking occurs after days instead of years. Very few experimental studies on the effect of creep on corrosion-induced surface cracking are available. In Alonso et al. (1998), a decrease of the corrosion rate (i.e., a decrease of the loading rate) has been shown to increase the crack opening, which was suggested to be related to creep. These results were obtained for the crack opening at the surface of the specimen, i.e., after surface cracking had already occurred. Similar results were also reported in more recent studies in Pedrosa and Andrade (2017).

The aim of the present study is to investigate the influence of long-term effects on corrosion-induced surface cracking by numerical modelling. Three models of increasing complexity are used, namely uncracked and cracked axis-symmetric thick-walled cylinder models and lattice models. Both the influence of basic creep and change of concrete maturity are studied. Migration of corrosion products into the adjacent concrete and compaction of the corrosion layer are not considered, so that the influence of long-term response of concrete can be isolated. To achieve this aim, a new perfectly plastic model for fracture of a thick-walled cylinder is derived. Furthermore, a new formulation for a cracked axis-symmetric thick-walled cylinder is developed. Finally, a new combination of a linear creep with a damage-plasticity constitutive model for a discrete approach is proposed. To investigate the effect of creep, thick-walled cylinder analyses were carried out for corrosion rates corresponding to accelerated and natural corrosion. Furthermore, to better understand the influence of maturity, the analyses were carried out for corrosion starting at 28 and 10000 days, with the former value corresponding to accelerated experiments carried out in a research laboratory and the latter corresponding to naturally occurring corrosion of matured concrete.

2 Modelling

The effect of creep on corrosion-induced cracking of concrete is investigated by modelling a thick-walled cylinder in plane stress, which represents the top layer of a cylindrical specimen with a single reinforcement bar in the centre. This setup is often used in accelerated corrosion tests. This idealised geometry was chosen so that three models of increasing complexity can be applied, two of which rely on the assumption of axial symmetry. The three models are

- an elastic axis-symmetric thick-walled cylinder model with a plastic limit,
- an inelastic axis-symmetric thick-walled cylinder model with advancing crack front, and
- a lattice model based on a three-dimensional discretisation of the thick-walled cylinder.

Because of the different levels of complexity, it is not expected that these models will predict the same amount of corrosion at surface cracking. Therefore, it is not attempted to calibrate the models to produce the same results. Instead, input parameters are chosen based on previous modelling and experiments.

During the corrosion process, steel is transformed into corrosion products which, because of their lower density, produce the mechanical loading on the thick-walled cylinder. The amount of corrosion products is measured in the form of a corrosion penetration, i.e., the thickness of the steel layer that has been transformed into corrosion products. For small penetrations compared to the steel bar diameter, the corrosion penetration is proportional to the corrosion current density:

$$\Delta x_{\text{cor}} = 0.0315 i_{\text{cor}} \Delta t \quad (1)$$

Here, Δx is the corrosion penetration in μm , i_{cor} is the corrosion current density in $\mu\text{A}/\text{cm}^2$, Δt is the time duration in days, and 0.0315 (in $10^{-4}\text{m}^3/(\text{A}\cdot\text{day})$) is a conversion factor based on Faraday's law (Bushman, 2000).

The focus of the present work is the effect of long-term behaviour of concrete, i.e., creep and change of maturity, on the initiation of surface cracking due to corrosion. To facilitate the assessment of the importance of the long-term behaviour, other effects such as migration and compaction of corrosion products, composition of rust products, shrinkage of concrete and external loading are not taken into account. At surface cracking, the corrosion layer Δx is so thin that it is acceptable to calculate the expansion as $\Delta u_{\text{cor}} = (\alpha - 1) \Delta x_{\text{cor}}$ where α is an expansion factor which is set here to 2 as used in many studies before, Molina et al. (1993). Therefore, $\Delta u_{\text{cor}} = \Delta x_{\text{cor}}$.

The corrosion current density i_{cor} is the main variable in this study. Setting $i_{\text{cor}} \geq 100 \mu\text{A}/\text{cm}^2$ provides conditions typically encountered in accelerated laboratory tests (Andrade et al., 1993), in which surface cracking of the cylinder is reached in a few days. In some accelerated tests in Mullard and Stewart (2009), even higher current densities up to $1000 \mu\text{A}/\text{cm}^2$ were used. On the other hand, $i_{\text{cor}} \leq 1 \mu\text{A}/\text{cm}^2$ corresponds to corrosion rates encountered in natural settings, where surface cracking is expected to be reached after several years (Broomfield, 1997). The main equations of the three modelling approaches are described in the following subsections. Special focus is on the description of creep modelling.

2.1 Uncracked axis-symmetric model with plastic limit

2.1.1 Original formulation

The first modelling approach is based on a combination of the elastic response of a thick-walled cylinder in plane stress combined with a plastic limit. It is commonly used as a mechanics based approach for predicting corrosion-induced cracking (Bažant, 1979a,b; Liu and Weyers, 1998). The main equations of the elastic model used here are reviewed and it is explained how creep and aging of concrete are considered.

For plane stress conditions, the constitutive equations linking strain and stress are

$$\begin{Bmatrix} \varepsilon_r \\ \varepsilon_\theta \end{Bmatrix} = \frac{1}{E''} \begin{pmatrix} 1 & -\nu \\ -\nu & 1 \end{pmatrix} \begin{Bmatrix} \sigma_r \\ \sigma_\theta \end{Bmatrix} \quad (2)$$

where r and θ are subscripts referring to the radial and circumferential direction in the cylindrical coordinate system as shown in Figure 1. Furthermore, ν is Poisson's ratio and E'' is the effective modulus, i.e., a modulus which takes into account the age at loading and the load duration and approximately replaces the viscoelastic operator. The stresses σ_r and σ_θ shown in Figure 1b satisfy the equilibrium condition

$$\frac{d\sigma_r}{dr} r + \sigma_r - \sigma_\theta = 0 \quad (3)$$

The strain components are linked to the radial displacement u by the kinematic relations

$$\varepsilon_r = \frac{du}{dr} \quad \text{and} \quad \varepsilon_\theta = \frac{u}{r} \quad (4)$$

Solving for the stresses in (2), setting them in to (3) and using kinematic relations in (4), the

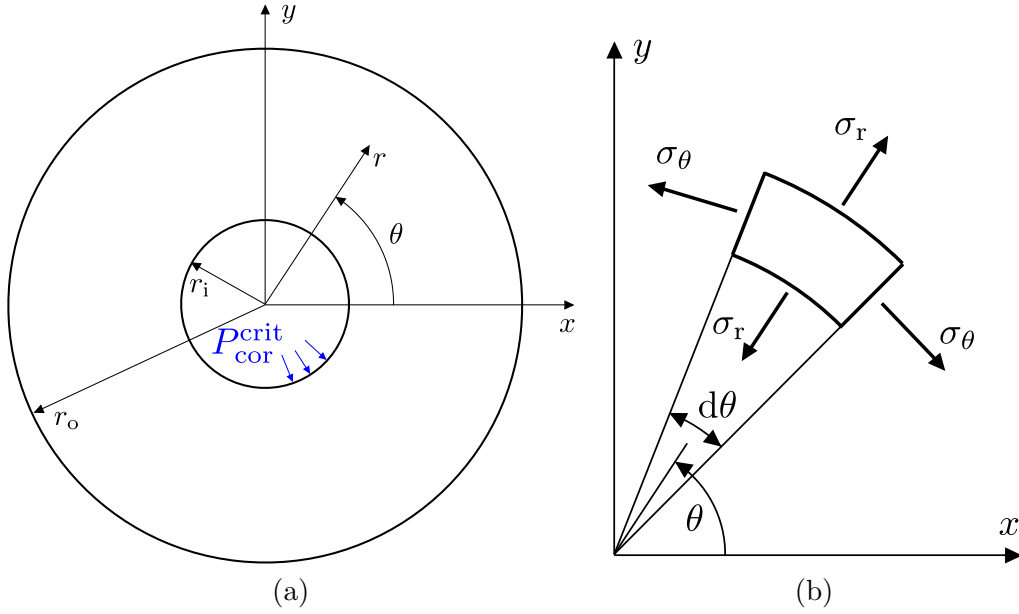


Figure 1: Uncracked cylinder with plastic limit: a) Geometry of the thick-walled cylinder in polar coordinate system and b) small member in equilibrium.

differential equation for the radial displacement u results in

$$\frac{d^2u}{dr^2} + \frac{1}{r} \frac{du}{dr} - \frac{u}{r^2} = 0 \quad (5)$$

This equation is combined with appropriate boundary conditions, which idealise the mechanical effect of the corrosion process. We assume that $\sigma_r = -P$ at $r = r_i$ and $\sigma_r = 0$ at $r = r_o$ (see Figure 1). Here, P is the pressure at the inner boundary of the cylinder induced by the formation of corrosion product (with compression considered as positive pressure). The solution of the boundary value problem reads

$$u(r) = \frac{P}{E''} \frac{((1-\nu)r^2 + (1+\nu)r_o^2) r_i^2}{(r_o^2 - r_i^2) r} \quad (6)$$

The displacement $u_i = u(r_i)$ induced at the inner boundary by pressure P can be expressed as

$$u_i = \frac{P}{E'' C} \quad (7)$$

where

$$C = \frac{r_o^2 - r_i^2}{((1-\nu)r_i^2 + (1+\nu)r_o^2) r_i} \quad (8)$$

is a geometry-dependent factor and the product $E'' C$ can be interpreted as the structural stiffness.

In the original version of the uncracked cylinder model, it is assumed that relation (7) is approximately valid also in the limit state, characterized by the critical pressure $P_{\text{cor}}^{\text{crit}}$ and the critical radial displacement u_i^{crit} . Therefore, we can write

$$P_{\text{cor}}^{\text{crit}} = E'' C u_i^{\text{crit}} \quad (9)$$

By introducing a plastic limit on the circumferential stress equal to the tensile strength f_t , we determine the critical pressure

$$P_{\text{cor}}^{\text{crit}} = f_t \frac{r_o - r_i}{r_i} \quad (10)$$

and combining this with (10) we get

$$u_i^{\text{crit}} = \frac{f_t}{E''C} \frac{r_o - r_i}{r_i} \quad (11)$$

The corrosion penetration at cracking is easily determined as $\Delta x_{\text{cor}}^{\text{crit}} = u_i^{\text{crit}}/(\alpha - 1)$. Finally, using the link between time and the penetration given by (1), we can evaluate the time at which the plastic limit is reached,

$$\Delta t^{\text{crit}} = \frac{u_i^{\text{crit}}}{0.0315(\alpha - 1)i_{\text{cor}}} = \frac{f_t}{0.0315(\alpha - 1)i_{\text{cor}}E''C} \frac{r_o - r_i}{r_i} \quad (12)$$

In (12), the effective modulus E'' and the tensile strength f_t are time-dependent. The effective modulus is determined using the modified Age-Adjusted Effective Modulus Method (Bažant, 1972; Bažant and Jirásek, 2018). The original formulation of the AAEM method in Bažant (1972) exhibits a singularity at $\Delta t = 0.01$ days, which is the loading duration for which the short term effective modulus is determined. This is not a problem if the load duration is much larger than 0.01 days. In the present study, we aim to investigate the effect of the corrosion density current including values which result in very short loading. To avoid any problems caused by the singularity, a modified expression for AAEM described in Example 4.5 in Bažant and Jirásek (2018) is used, which provides $E'' = E^{28}$ for $\Delta t_s = 0.01$ days, where E^{28} is the Young modulus at 28 days for a loading duration of $t = 0.01$ days. In this method, the effective modulus E'' is given as

$$E''(t, t_0) = \frac{1 - R(t, t_0)J(t_0^*, t_0)}{J(t, t_0) - J(t_0^*, t_0)} \quad (13)$$

where

$$t_0^* = \begin{cases} 0.9t_0 + 0.1t & \text{if } t_0 < t < t_0 + 10\Delta t_s \\ t_0 + \Delta t_s & \text{if } t_0 + 10\Delta t_s \leq t \end{cases} \quad (14)$$

and t_0 is the time at which loading starts. In (13), the relaxation function R is approximated according to Bažant and Jirásek (2018) as

$$R(t, t_0) = \frac{1}{J(t, t_0)} \left[1 + \frac{c_1(t_0)J(t, t_0)}{10J(t, t - \Delta t)} \left(\frac{J(t_m, t_0)}{J(t, t_m)} - 1 \right) \right]^{-10} \quad (15)$$

where $\Delta t = 1$ day, $t_m = (t + t_0)/2$, and

$$c_1(t_0) = 0.08 + 0.0119 \ln t_0 \quad (16)$$

The compliance function J in (13) and (15) is chosen according to the B3 model originally proposed in Bažant and Baweja (1994) and described in Section C.1 in Bažant and Jirásek (2018) as

$$J(t, t_0) = q_1 + q_2 Q(t, t_0) + q_3 \ln [1 + (t - t_0)^n] + q_4 \ln \left(\frac{t}{t_0} \right) \quad (17)$$

Here, q_1 , q_2 , q_3 and q_4 are creep parameters of the B3 model, $n = 0.1$ and Q is a special function defined by an integral formula, which can be evaluated numerically or approximated analytically. Only basic creep is considered, i.e., shrinkage and drying creep are ignored.

The dependence of the tensile strength on the age of concrete is taken into account using the *fib* Model Code 2010. Two expressions in this code are used. Firstly, formula

$$f_c(t) = f_c^{28} \exp\left(s \left[1 - \sqrt{28/t}\right]\right) \quad (18)$$

describes the increase in compressive strength with increasing age of the concrete. Here, f_c^{28} is the compressive strength at 28 days, s is a parameter that depends on the aggregate type and t is the concrete age substituted in days. Secondly, the Model Code 2010 expression which relates tensile and compressive strengths is used to calculate the tensile strength at time t and 28 days using $f_c(t)$ and f_c^{28} , respectively. The ratio of these two tensile strength values is then multiplied with the reference tensile strength to obtain the tensile strength at time t . Reduction of the tensile strength due to nonlinear creep was not taken into account.

Setting (13) and (18) in (12), a nonlinear equation for t^{crit} is obtained. An interactive method is then used to solve for t^{crit} and then to determine $x_{\text{cor}}^{\text{crit}}$ using (1). The calibration of the model is discussed in Section 3.

2.1.2 Improved formulation

The simple version of the thick cylinder model used in the literature and presented in the previous subsection is based on a somewhat inconsistent set of assumptions: Relation (9) that links the radial pressure on the internal boundary to the radial displacement is derived assuming linear (visco)elastic behavior but the limit value of the pressure (10) is obtained from equilibrium in the plastic limit state, in which the circumferential stress in the whole cylinder is at the yield limit, f_t . Of course, to reach this stress distribution, the plastic zone must spread from the inner boundary to the whole cylinder and the developed nonuniform plastic strains contribute to the overall deformation of the cylinder and thus also to the boundary displacement. Under certain reasonable assumptions, the stresses, strains and displacements in the plastic limit state can be evaluated analytically, as will be shown next.

The assumption that the circumferential stress in the plastic limit state is uniform and equal to the tensile yield stress naturally corresponds to the Rankine yield condition, based on the maximum principle stress. When the expected circumferential stress distribution $\sigma_\theta(r) = f_t$ is substituted into the equilibrium equation (3), one gets a differential equation

$$\frac{d\sigma_r}{dr} r + \sigma_r = f_t \quad (19)$$

from which the radial stress can be obtained. Since the left-hand side of (19) corresponds to the derivative $d(r\sigma_r)/dr$, integration is easy and leads to

$$\sigma_r = f_t + \frac{C_1}{r} \quad (20)$$

When the integration constant $C_1 = -r_o f_t$ is determined from the boundary condition $\sigma_r(r_o) = 0$, it turns out that the radial stress distribution in the plastic limit state is described by

$$\sigma_r = f_t \left(1 - \frac{r_o}{r}\right) \quad (21)$$

The second boundary condition, $\sigma_r(r_i) = -P_i$, can be used to evaluate the radial pressure P on the internal boundary in the plastic limit state. Interestingly, the result exactly corresponds to the pressure $P_{\text{cor}}^{\text{crit}}$ given by formula (10). This is of course due to the fact that the global equilibrium condition from which (10) was derived can be constructed by integrating equation (19) from r_i to r_o and substituting $\sigma_r(r_i) = -P_{\text{cor}}^{\text{crit}}$ and $\sigma_r(r_o) = 0$.

The next step is to proceed from stresses to strains. For the plastic part of the model based on the Rankine yield condition, it is natural to use the associated flow rule. Note that the radial stress σ_r given by (21) is negative inside the whole interval (r_i, r_o) . This confirms the assumption that $\sigma_\theta = f_t$ is the maximum principal stress, and the flow rule associated with the Rankine condition predicts plastic flow with $\varepsilon_{\theta p} > 0$ and $\varepsilon_{r p} = 0$. The total strains are the sum of these plastic strain components and the elastic strain components evaluated from the already known stresses using (2). The resulting expressions are

$$\varepsilon_r = \frac{f_t}{E''} \left(1 - \nu - \frac{r_o}{r}\right) \quad (22)$$

$$\varepsilon_\theta = \frac{f_t}{E''} \left(1 - \nu + \frac{\nu r_o}{r}\right) + \varepsilon_{\theta p} \quad (23)$$

where the plastic strain $\varepsilon_{\theta p}$ is yet to be determined.

The strain components are both linked to one displacement function, u , and so they must satisfy a certain compatibility condition. From the kinematic equations (4) we get $du/dr = \varepsilon_r$ and $u = r\varepsilon_\theta$, which can be simultaneously true only if

$$\varepsilon_r = \frac{d}{dr} (r\varepsilon_\theta) \quad (24)$$

Substituting from (22)–(23) and rearranging, we obtain a differential equation

$$\frac{d}{dr} (r\varepsilon_{\theta p}) = -\frac{f_t}{E''} \frac{r_o}{r} \quad (25)$$

from which the plastic strain can be evaluated. The general solution reads

$$\varepsilon_{\theta p} = -\frac{f_t r_o}{E''} \frac{\ln r}{r} + \frac{C_2}{r} \quad (26)$$

The integration constant C_2 needs to be determined from a suitable boundary condition. We are interested in the state at the onset of plastic collapse, when the complete yield mechanism has just developed. Therefore, there must be a point at which the stress has just reached the yield limit and the plastic strain is still zero while all other points are at a positive plastic strain. The plastic zone is expected to progress from the inner surface, and thus it can be expected that the point that yields last is located at the outer surface. Condition $\varepsilon_{\theta p}(r_o) = 0$ leads to $C_2 = (f_t/E'') r_o \ln r_o$ and

$$\varepsilon_{\theta p} = \frac{f_t}{E''} \frac{r_o}{r} \ln \frac{r_o}{r} \quad (27)$$

Substituting this back into (23) and using the kinematic equation, we can evaluate the displacement function

$$u = r\varepsilon_\theta = \frac{f_t}{E''} ((1 - \nu)r + \nu r_o) + r\varepsilon_{\theta p} = \frac{f_t}{E''} \left((1 - \nu)r + \left(\nu + \ln \frac{r_o}{r} \right) r_o \right) \quad (28)$$

Specifically, the displacement at the inner boundary in the plastic limit state is given by

$$u_i^{\text{plast}} = \frac{f_t}{E''} \left((1 - \nu)r_i + \left(\nu + \ln \frac{r_o}{r_i} \right) r_o \right) \quad (29)$$

This consistently evaluated displacement can be related to the pressure in the plastic limit state by a formula of the same kind as (9), just with a modified geometry factor

$$C^{\text{plast}} = \frac{P_{\text{cor}}^{\text{crit}}}{E'' u_i^{\text{plast}}} = \frac{r_o - r_i}{\left((1 - \nu)r_i + \left(\nu + \ln \frac{r_o}{r_i} \right) r_o \right) r_i} \quad (30)$$

Same as for the original model, this modified factor is used in (12) considered as a nonlinear equation from which the time to cracking can be evaluated. The modified formula gives a lower stiffness than the original formula because the contribution of plastic yielding to the overall compliance is taken into account. It can therefore be expected that the resulting times to cracking will be longer.

2.2 Cracked axis-symmetric model

The next formulation used in this study is for a cracked axis-symmetric thick-walled cylinder. In this model, the cylinder is split into a cracked and uncracked part. The limit on the inner pressure is obtained automatically by increasing incrementally the radius of the cracked cylinder. The way how cracking is introduced is conceptually based on previous work in Grassl et al. (2019) in which the initiation of fluid-induced fracture of a thick-walled hollow permeable sphere was modelled. Here, it is presented for the first time for an impermeable thick-walled axis-symmetric cylinder. The amount of corrosion penetration required to induce surface cracking is strongly dependent on the stiffness of the surrounding material. Therefore, considering the cracking process within the cylinder is important. Within an axis-symmetric thick-walled cylinder formulation, cracking is considered by introducing a cracking strain. Many of the equations are the same as in the previous elastic modelling approach. Here, the main differences are pointed out.

The geometry of the cracked thick-walled cylinder is shown in Figure 2a. The stress-strain equations

$$\begin{Bmatrix} \varepsilon_r \\ \varepsilon_\theta \end{Bmatrix} = \frac{1}{E''} \begin{pmatrix} 1 & -\nu \\ -\nu & 1 \end{pmatrix} \begin{Bmatrix} \sigma_r \\ \sigma_\theta \end{Bmatrix} + \begin{Bmatrix} 0 \\ \varepsilon_\theta^{\text{cr}} \end{Bmatrix} \quad (31)$$

are an extension of the elastic law (2) and incorporate the cracking strain $\varepsilon_\theta^{\text{cr}}$. Before crack initiation, the cracking strain is zero. The crack is initiated when the circumferential stress attains the tensile strength, f_t . After crack initiation, the cracking strain $\varepsilon_\theta^{\text{cr}}$ is linked to the circumferential stress σ_θ by the exponential softening law (Figure 2b) as

$$\sigma_\theta = f(\varepsilon_\theta^{\text{cr}}, r) \equiv f_t \exp\left(-\frac{\varepsilon_\theta^{\text{cr}}}{\varepsilon_f}\right) \quad (32)$$

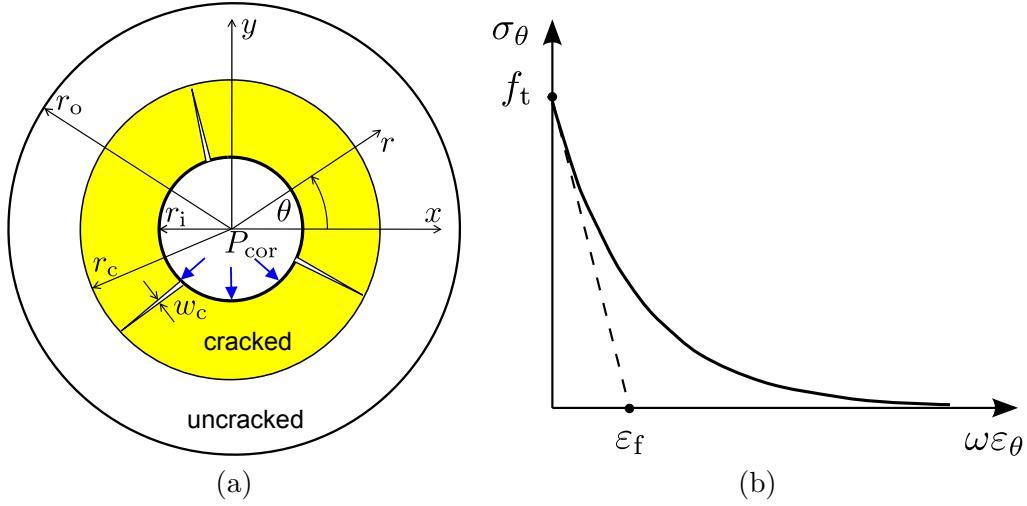


Figure 2: Cracked cylinder: a) Geometry of the thick-walled cylinder split into a cracked and uncracked part and b) stress-cracking strain softening law.

where $\varepsilon_f = n_c G_f / (f_t 2\pi r)$ is a characteristic cracking strain. The number of radial cracks n_c is one of the input parameters of the model. The equilibrium and kinematic equations are the same as in (3) and (4), respectively.

Solving (31) for σ_r and σ_θ , setting the stresses into (3) and using the kinematic equations in (4) gives

$$\frac{d^2 u}{dr^2} + \frac{1}{r} \frac{du}{dr} - \frac{1}{r^2} u + \frac{1}{r} (1 - \nu) \varepsilon_\theta^{\text{cr}} - \nu \frac{d\varepsilon_\theta^{\text{cr}}}{dr} = 0 \quad (33)$$

Here, the term $d\varepsilon_\theta^{\text{cr}}/dr$ is solved by differentiating (32) with respect to r , which provides

$$\frac{d\varepsilon_\theta^{\text{cr}}}{dr} = \frac{1}{A} \left(\frac{du}{dr} \frac{1}{r} - \frac{u}{r^2} + \nu \frac{d^2 u}{dr^2} \right) \quad (34)$$

Here, the factor A is

$$A = 1 - \frac{f_t}{E\varepsilon_f} (1 - \nu^2) \exp\left(-\frac{\varepsilon_\theta^{\text{cr}}}{\varepsilon_f}\right) \quad (35)$$

Setting the expression for the derivative of the cracking strain in (34) into (33) gives the nonlinear ordinary differential equation of the form

$$\frac{d^2 u}{dr^2} + \frac{1}{r} \frac{du}{dr} \frac{A - \nu}{A - \nu^2} - \frac{1}{r^2} u \frac{A - \nu}{A - \nu^2} + \frac{1}{r} \frac{A(1 - \nu)}{A - \nu^2} \varepsilon_\theta^{\text{cr}} = 0 \quad (36)$$

whereby the cracking strain $\varepsilon_\theta^{\text{cr}}$ is defined implicitly by the nonlinear differential equation in (32). The boundary conditions are the same as for the uncracked model. A constant radial displacement rate at the inner boundary is prescribed and the traction at the outer boundary is assumed to vanish. The nonlinear equation in (36) with $\varepsilon_\theta^{\text{cr}}$ in (32) is solved using MATLAB with the boundary value solver `bvp4c`.

2.3 Lattice modelling

This section describes the lattice modelling approach for corrosion-induced cracking. The approach is a combination of previously developed lattice models based on a damage-plasticity constitutive model, presented previously in Grassl and Davies (2011); Athanasiadis et al. (2018), and the linear creep model proposed in Jirásek and Havlásek (2014) based on micro-prestress solidification theory of concrete creep. The new contribution in the present work is the combination of these two modelling concepts. This modelling approach is too complex to allow us to present all the equations in detail as it was done for the uncracked and cracked axis-symmetric models. Instead, the overall concept is introduced and only the combination of the damage-plasticity model and the linear creep model is presented in more detail.

The spatial discretisation is based on sequentially placed random vertices while enforcing a minimum distance. These vertices are used for dual Delaunay and Voronoi tessellations (Yip et al., 2005). The random vertices form the nodes of the lattice element (see vertices i and j in Figure 3a). The edges of the Delaunay tetrahedra are used for the connections of the nodes, i.e. the edges give the location of the lattice elements. The mid-cross-section of the lattice elements is obtained from the facets of the Voronoi polyhedra. Boundaries of the specimen are modelled using mirrored vertices as described in Yip et al. (2005). Each node has six degrees of freedom, namely three translations and three rotations. These nodal degrees of freedom are used to compute translational displacement jumps at the centroid of the mid-cross-section of the element by means of rigid body kinematics assuming that the two nodes of an element belong to two rigid polyhedra which meet at the facet which forms the mid-cross-section (Figure 3b). The translational displacement jump is transformed into strain by dividing them by the element length. This strain is used as an input for the constitutive model to compute the stress, which is then related to the nodal forces. No rotational stiffness at point C is considered. The constitutive model is described in more detail in the following section.

2.3.1 Damage plasticity model with extension to visco-elasticity

For the damage plasticity model, the plasticity part uses a yield surface which is a function of the normal component and the norm of the two shear components of the effective stress. Geometrically, the surface is composed of two ellipses, so that there are limits on the normal component of the effective stress both in tension and in compression (Figure 3c). Plastic flow is modelled with a plastic potential which differs from the yield function, so that the amount of normal plastic strain can be controlled. Damage is determined from the positive normal component of the plastic strain using an exponential softening law (Figure 3d). The damage-plasticity model uses nine parameters. Parameters E and a_1 control the macroscopic Young's modulus and Poisson's ratio of the material. Additional parameters, f_t , f_c , α_c , β_c and A_h , determine the shape and size of the yield surface and its evolution during hardening. Furthermore, parameter ψ controls the plastic flow. Finally, G_F controls the amount of energy dissipated during cracking.

For the standard damage plasticity approach, the stress-dependent strain vector is defined as $\boldsymbol{\varepsilon}_\sigma = \boldsymbol{\varepsilon} - \boldsymbol{\varepsilon}_{\text{cor}}$ where $\boldsymbol{\varepsilon}$ is the total strain and $\boldsymbol{\varepsilon}_{\text{cor}}$ is the eigenstrain which reflects the formation of corrosion products. Using first the plasticity part of the damage-plasticity model, the effective stresses $\bar{\boldsymbol{\sigma}}$,

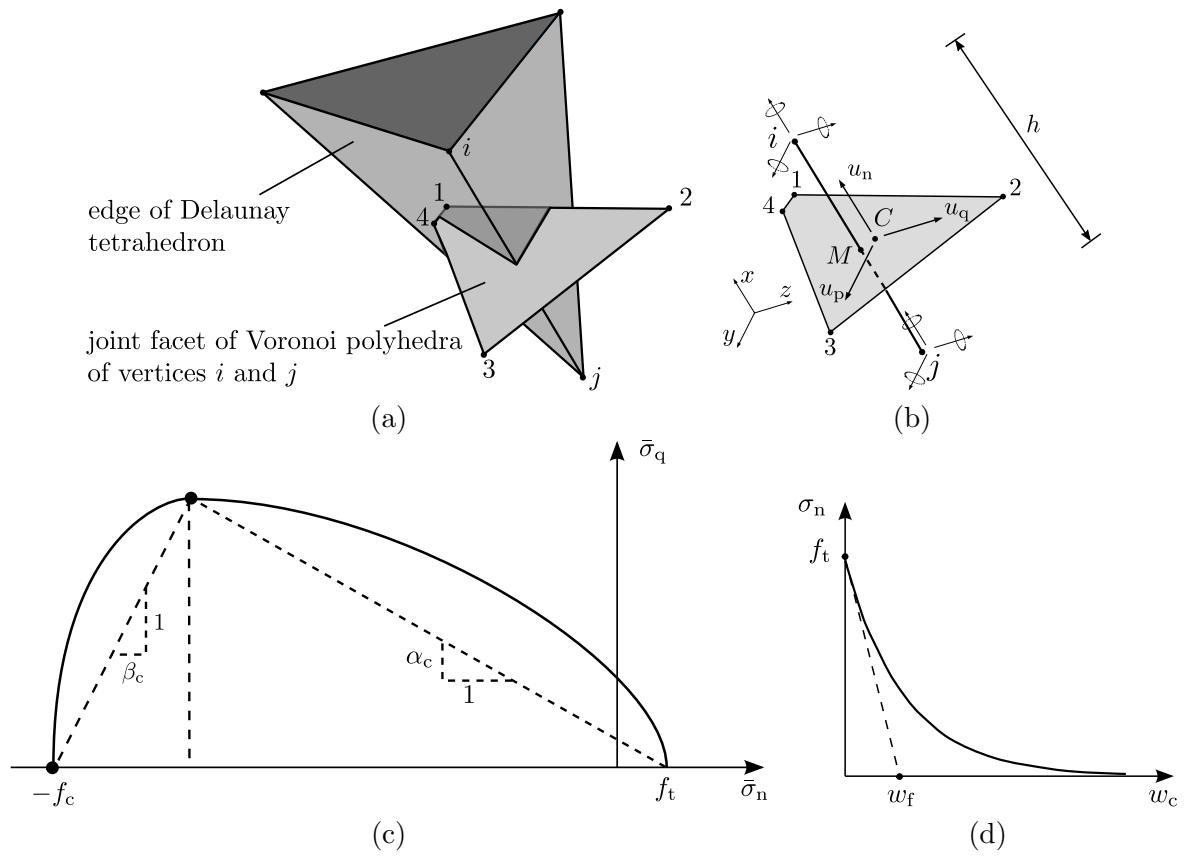


Figure 3: Lattice model: a) geometrical relationship between Delaunay and Voronoi tessellations, b) lattice element with cross-section defined by the associated Voronoi facet, c) yield surface, and d) exponential softening law.

plastic strain $\boldsymbol{\varepsilon}_p$ and hardening variable κ_p are computed. All these quantities are independent of damage. Subsequently, the damage parameter ω is determined using the results of the plasticity part. The nominal stress is determined as

$$\boldsymbol{\sigma} = (1 - \omega) \mathbf{D}_e (\boldsymbol{\varepsilon}_\sigma - \boldsymbol{\varepsilon}_p) = \mathbf{D}_e (\boldsymbol{\varepsilon}_\sigma - \boldsymbol{\varepsilon}_p - \omega (\boldsymbol{\varepsilon}_\sigma - \boldsymbol{\varepsilon}_p)) \quad (37)$$

Here, the inelastic strain which is subtracted from the stress-dependent strain $\boldsymbol{\varepsilon}_\sigma$ consists of an irreversible part in the form of the plastic strain $\boldsymbol{\varepsilon}_p$ and a reversible part in the form of the damage strain

$$\boldsymbol{\varepsilon}_\omega = \omega (\boldsymbol{\varepsilon}_\sigma - \boldsymbol{\varepsilon}_p) \quad (38)$$

For the visco-elastic extension of the damage-plasticity model, we consider the special case of constant ambient temperature under hygrally sealed conditions. For this case, the response of the visco-elastic model is identical to the basic creep compliance function of the B3 model. The implementation of the MPS material model uses the rate-type approach summarised in “Algorithm 10.1: Incremental stress–strain relation according to the microprestress-solidification theory” (Bažant and Jirásek, 2018). Under sealed conditions this algorithm can be further simplified to “Algorithm 5.3: Exponential algorithm for solidifying Kelvin chain”. Additionally, the parameters of the Dirichlet series are estimated from the continuous retardation spectrum (Jirásek and Havlásek, 2014) of the non-aging compliance function, which makes the implementation more efficient.

The visco-elastic extension of the damage-plasticity approach models the evolution of tensile and compressive strength with time described by the *fib* Model Code 2010 formulae (Fédération Internationale du Béton, 2012). The viscoelastic model and the damage-plasticity model are linked in series. This implies that the stress transmitted by the two models needs to be equal and the (stress-dependent) total strain $\boldsymbol{\varepsilon}_\sigma$ needs to be split into viscoelastic $\boldsymbol{\varepsilon}_{ve}$ and inelastic components $\boldsymbol{\varepsilon}_{pl}$ and $\boldsymbol{\varepsilon}_\omega$. Owing to the viscoelastic nature of the problem, the stiffness matrix is no longer constant and is proportional to the incremental modulus E . For simplicity, the stiffness which is used in the plasticity-damage part of the model is assumed as a constant and is evaluated from the basic creep compliance function using the expression for the conventional Young’s modulus at the age of 28 days for a load duration of 0.01 days ($E_{28} = 1/J_b(28.01, 28)$). In the first step, the stress-dependent strain vector associated with the viscoelastic material is computed as

$$\boldsymbol{\varepsilon}_{ve,\sigma} = \boldsymbol{\varepsilon} - \boldsymbol{\varepsilon}_{cor} - (\boldsymbol{\varepsilon}_p + \boldsymbol{\varepsilon}_\omega) \quad (39)$$

where $\boldsymbol{\varepsilon}_\omega$ and $\boldsymbol{\varepsilon}_p$ are the temporary values of damage and plastic strain vectors, respectively, which will be updated during the iterative process. The stress-dependent strain vector $\boldsymbol{\varepsilon}_{ve,\sigma}$ is then used in the stress-evaluation algorithm of the viscoelastic model and the stress $\boldsymbol{\sigma}_{ve}(\boldsymbol{\varepsilon}_{ve,\sigma})$ is computed. This is the nominal stress, which needs to be equal to the nominal stress determined by the damage-plasticity model since the two models are combined in series. Therefore, as the next step, the stress-dependent part of the strain vector associated with the plasticity-damage material is computed as

$$\boldsymbol{\varepsilon}_\sigma = \mathbf{D}_{28}^{-1} \boldsymbol{\sigma}_{ve} + \boldsymbol{\varepsilon}_\omega + \boldsymbol{\varepsilon}_p \quad (40)$$

where \mathbf{D}_{28} is the stiffness matrix that corresponds to the conventional elastic modulus, E_{28} . Strain $\boldsymbol{\varepsilon}_\sigma$ is then used for the damage-plasticity model following the steps outlined for the standard version

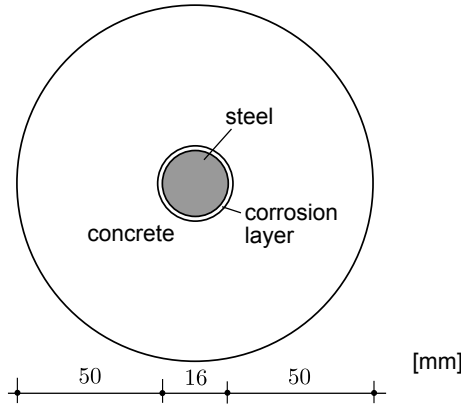


Figure 4: Geometry of the thick-walled cylinder analysed with the three approaches. The out-of-plane thickness is 10 mm.

of that model. The nominal stress obtained from the damage-plasticity approach is compared to nominal stress obtained from the visco-elastic model. If the difference between these two nominal stresses exceeds a prescribed tolerance, the two nominal stresses are calculated again whereby the viscoelastic nominal stress is now determined with a new strain which considers the new plastic and damage parts of the inelastic strains. This procedure is repeated until the stresses obtained using the two models are the same.

3 Analyses

The three modelling approaches described in the previous section (uncracked and cracked axis-symmetric model, and lattice model) are calibrated using short-term material properties of a reference concrete at 28 days with Young's modulus $E^{\text{ref}} = 30$ GPa, Poisson's ratio $\nu^{\text{ref}} = 0.2$, tensile strength $f_t^{\text{ref}} = 3$ MPa, compressive strength $f_c^{\text{ref}} = 30$ MPa and fracture energy $G_F^{\text{ref}} = 150$ N/m. The reference Young's modulus corresponds to an effective modulus with a load duration of 0.01 days at loading start time of 28 days. In the following paragraphs, the geometry and boundary conditions of the problem, the calibration procedure and the results obtained with the three approaches are presented.

3.1 Geometry and boundary conditions

The geometry of the problem analysed consists of a concrete cylinder with a steel reinforcement bar at its centre. The radius of the reinforcement bar is $r_i = 8$ mm and the outer radius of the concrete cylinder is $r_o = 58$ mm as shown in Figure 4. The out of plane thickness is 10 mm. This slice of thick-walled cylinder represents the region of a test specimen close to the free boundary. Therefore, plane stress conditions are assumed for the two axis-symmetric models. For the lattice model, the 3D slice was discretised and the nodes of the lattice were not restrained in the out-of-plane direction. For the two axis-symmetric models, the corrosion process is modelled by prescribing an outwards radial displacement at the inner boundary of the concrete cylinder. This assumes that the steel reinforcement bar is so stiff that its deformation does not influence the results. For

the lattice model, it was more straight-forward to discretise the steel bar as well and model the radial displacement induced by the formation of the corrosion products by a layer of the lattice elements adjacent of the steel bar, whereby the elements are arranged so they are perpendicular to the circumference of the steel bar. Within this layer of lattice elements the expansion due to the formation of the corrosion products was modelled by an eigenstrain computed from a prescribed eigen-displacement, which was determined for all approaches using (1) and the assumption that $u_{\text{cor}} = x_{\text{cor}}$, i.e. $\alpha = 2$. This approach makes the radial displacement independent of the lattice element length. The main variable investigated is the corrosion rate i_{cor} . Analyses with the elastic-axisymmetric and lattice models for different corrosion current densities $i_{\text{cor}} = 0.1, 1, 10, 100, 1000$ and $10000 \mu\text{A}/\text{cm}^2$ are performed to determine the amount of corrosion penetration at which the maximum internal pressure, which is called strength of the thick-walled cylinder, is reached. For most analyses, surface cracking is reached at this critical corrosion penetration. In general, the smaller the corrosion current density, the greater is the time at which the strength is reached. However, interplay of creep and change of maturity affects the time to cracking, too. To better understand the influence of maturity, the analyses were carried out for $t_0 = 28$ and 10000 days with the former corresponding to accelerated experiments carried out in a research laboratory and the latter corresponding to naturally occurring corrosion of matured concrete.

3.2 Calibration

The calibration procedures for the three models are described below. For the uncracked thick-walled cylinder model with plastic limit, the model parameters are ν^{ref} , f_t^{ref} , q_1 , q_2 , q_3 and q_4 . The first two parameters can be chosen directly from the properties of the reference concrete, which are $\nu^{\text{ref}} = 0.2$ and $f_t^{\text{ref}} = 3 \text{ MPa}$. The four parameters for basic creep are determined in two steps. Firstly, an initial set of parameters are calculated using the formulas in Bažant and Baweja (1995), assuming concrete mix composition as water $w = 180 \text{ kg}/\text{m}^3$, cement $c = 360 \text{ kg}/\text{m}^3$ and aggregate $a = 1860 \text{ kg}/\text{m}^3$. These formulas estimate the elastic modulus from the compressive strength based on an empirical formula suggested by the ACI recommendations, and so the resulting modulus differs from the Young modulus of the reference concrete at 28 days for a loading duration of 0.01 days. In the present study, both reference compressive strength and reference Young's modulus are given. To obtain the desired reference Young modulus E^{ref} , the four parameters q_1 to q_4 are scaled by the same factor. The resulting creep parameters are $q_1 = 19.367 \times 10^{-6}/\text{MPa}$, $q_2 = 137.865 \times 10^{-6}/\text{MPa}$, $q_3 = 2.499 \times 10^{-6}/\text{MPa}$ and $q_4 = 5.381 \times 10^{-6}/\text{MPa}$. The cracked thick-walled cylinder model uses the same parameters as the uncracked cylinder model, but requires two additional parameters—the fracture energy G_F and the number of cracks n_c . The fracture energy is set to $G_F^{\text{ref}} = 150 \text{ N}/\text{m}$. The number of cracks needs to be assumed, which is one of the disadvantages of the cracked thick-walled cylinder model. In this study, we use $n_c = 4$, which was used before in Fahy et al. (2017) for a similar model covering the special case of Poisson's ratio $\nu = 0$.

The parameters of the lattice approach are calibrated in multiple steps. Firstly, the parameters E and a_1 of the lattice model are determined from a direct tensile test so that the reference elastic properties $E^{\text{ref}} = 30 \text{ GPa}$ and $\nu^{\text{ref}} = 0.2$ are obtained. These analyses were initially carried out without taking creep into account. The specimen used for the direct tensile test has a length of 75 mm, width of 50 mm and an out-of plane thickness of 10 mm. The load was applied in the long

direction of the specimen. The values of the two parameters are determined as $E = 45.91$ GPa and $a_1 = 0.297$. Next, the creep parameters of the B3 model q_1 to q_4 are determined on a single element subjected to uniaxial tension using the same approach as for the uncracked and cracked cylinder models, namely first determining the parameters using the formulas in Bažant and Baweja (1995) and then scaling them to obtain the lattice material Young’s modulus E . This is the same approach that was used for the two axis-symmetric models, with the difference that the target Young’s modulus for the lattice approach is $E = 45.91$ GPa. The resulting values of the creep parameter for the lattice model are $q_1 = 12.640 \times 10^{-6}/\text{MPa}$, $q_2 = 89.982 \times 10^{-6}/\text{MPa}$, $q_3 = 1.631 \times 10^{-6}/\text{MPa}$ and $q_4 = 3.512 \times 10^{-6}/\text{MPa}$. For the single element, the load is applied instantaneously at $t_0 = 28$ days and the secant modulus is determined at a duration of $\Delta t = 0.01$ days. Next, the inelastic parameters are determined, so that f_t^{ref} and G_f^{ref} are obtained. This calibration is carried out on the direct tensile test which was used earlier for obtaining the elastic properties. To avoid fracture at the boundaries, the end regions were set to be elastic so that only a middle region of 50 mm was able to fracture. The lattice model considers the randomness of the material strength by an autocorrelated random field with a Gaussian probability function of fully correlated strength and fracture energy (Grassl and Jirásek, 2010). The autocorrelation length is chosen as $l_a = 2.67$ mm. Furthermore, the coefficient of variation of the random field is $c_v = 0.2$. Six analyses with random fields and meshes were carried out for this calibration step. The input parameters of the lattice model f_t and w_f were chosen so that mean tensile strength and fracture energy determined from the six analyses agreed with the reference properties. The resulting input parameters are $f_t = 2.35$ MPa and $w_f = 0.02$ mm. The other parameters of this lattice model are set to their default values as described in the manual of OOFEM (Patzák, 2012).

3.3 Results

The main set of results of this study is the dependence of the critical corrosion penetration $x_{\text{cor}}^{\text{crit}}$ on the corrosion current density i_{cor} . For the uncracked thick-walled cylinder model, the critical corrosion penetration $x_{\text{cor}}^{\text{crit}}$ is the direct output of the calculation method. For the other two models, the critical corrosion penetration is obtained from the peak of the pressure corrosion penetration curve. The peak coincides with the stage at which the deformations localise and the cracks reach the surface of the thick-walled cylinder. This process is illustrated for $i_{\text{cor}} = 100$ and $1 \mu\text{A}/\text{cm}^2$ in Figures 5 and 6 for $t_0 = 28$ and 10000 days, respectively. The result of the two versions of the uncracked cylinder model are shown as isolated points, since in this model only the critical corrosion penetration is determined. For the lattice model, the result of one of the six random analyses is shown so that the crack patterns depicted in Figure 7 can be directly linked to points in the pressure-penetration curve. The pressure in Figures 5 and 6 is normalised by $f_t^{\text{ref}}(r_o - r_i)/r_i$, which corresponds to the pressure equilibrated by constant circumferential stress equal to the tensile strength f_t^{ref} . The crack patterns obtained from the lattice model with $i_{\text{cor}} = 100 \mu\text{A}/\text{cm}^2$ and $t_0 = 28$ days at stages marked in Figure 5 are shown in Figure 7. These crack patterns are representative of the other lattice analyses with different i_{cor} values and starting age $t_0 = 10000$ days. During the first stage, cracking is rather distributed. Then, one dominant crack forms and propagates to the specimen boundary. At the peak pressure, the crack is almost connected to the boundary, which changes the deformed shape of the cylinder significantly. Based on the evolution of the crack patterns, the peak of the pressure versus corrosion penetration curve is a good criterion for surface

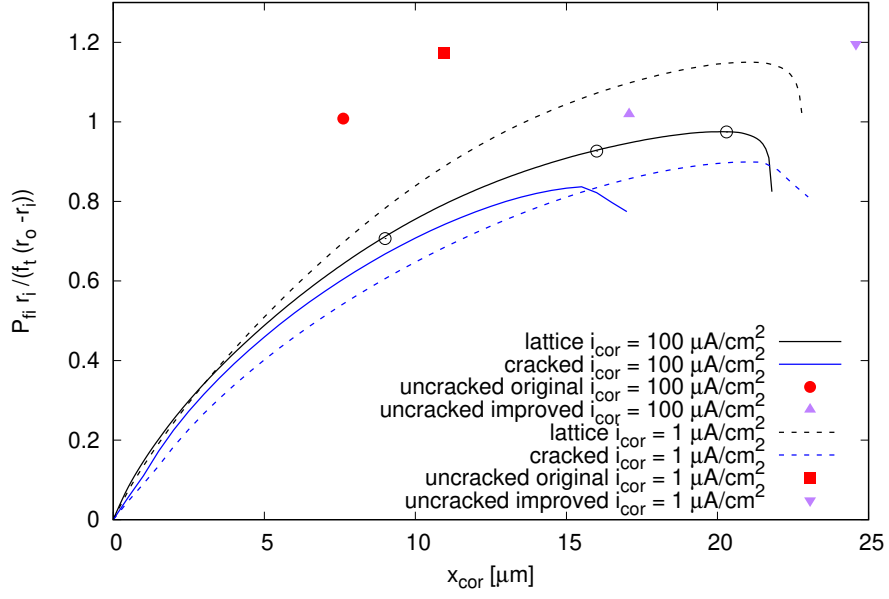


Figure 5: Normalised pressure at inner boundary versus corrosion penetration x_{cor} for $t_0 = 28$ days. The symbols on the lattice curve mark stages at which crack patterns are shown in Figure 7.

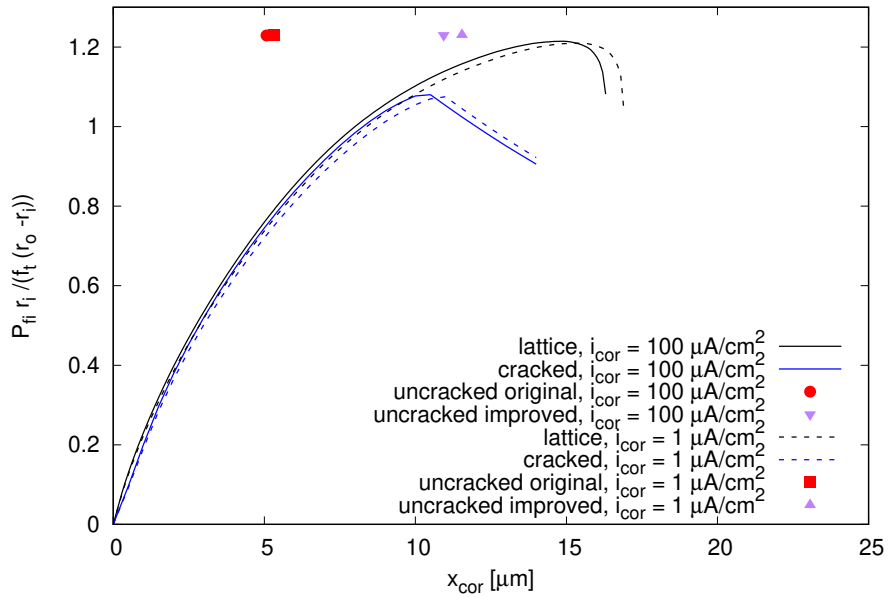


Figure 6: Normalised pressure at inner boundary versus corrosion penetration x_{cor} for $t_0 = 10000$ days.

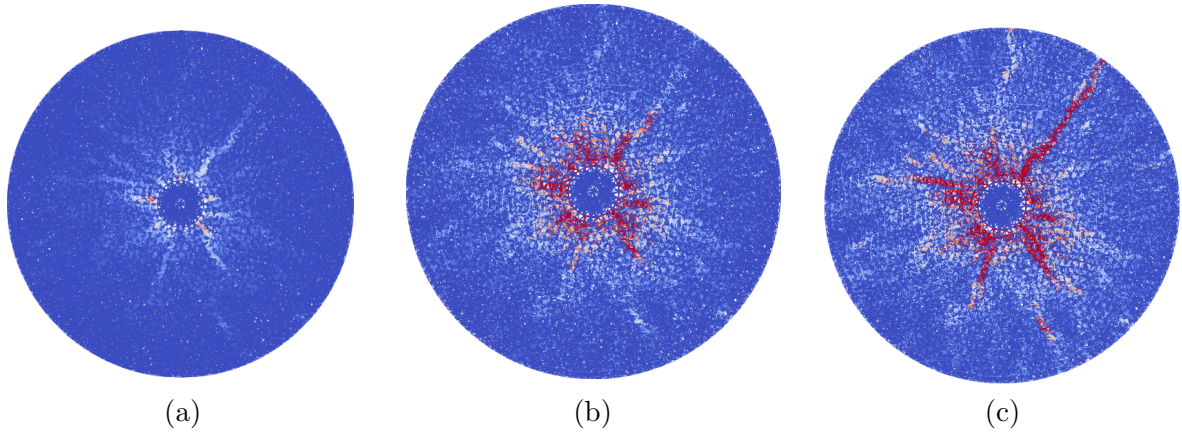


Figure 7: Crack patterns of lattice analyses: (a)-(c) three steps marked in Figure 5. Mid-cross-sections of lattice elements with crack openings greater than $2 \mu\text{m}$ are shown in red.

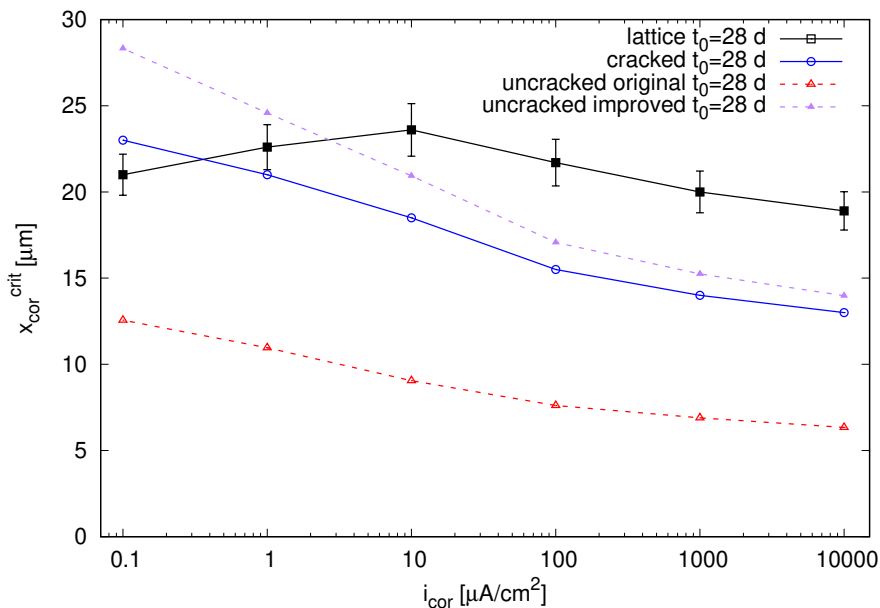


Figure 8: Critical penetration depth $x_{\text{cor}}^{\text{crit}}$ versus corrosion rate i_{cor} for loading at age $t_0 = 28$ days.

cracking. The corrosion penetration at peak will be considered as the critical corrosion penetration $x_{\text{cor}}^{\text{crit}}$.

The critical corrosion penetration versus the corrosion rate is presented for the two starting ages $t_0 = 28$ and 10000 days in Figures 8 and 9 for the three modelling approaches. For the lattice model, the results are the average of six random analyses. The error bars in the figures indicate the \pm standard deviation. The results for $t_0 = 28$ days in Figure 8 show that the effect of i_{cor} depends strongly on the modelling approach. For the uncracked model, i_{cor} has a very strong effect on the critical corrosion penetration. For $i_{\text{cor}} = 0.1 \mu\text{A}/\text{cm}^2$, $x_{\text{cor}}^{\text{crit}}$ is about twice the value for $i_{\text{cor}} = 1000 \mu\text{A}/\text{cm}^2$. This strong effect is also visible for the cracked model, but not for the lattice model. With the lattice model, the critical corrosion penetration first increases and then decreases with decreasing corrosion current density. The difference between the critical corrosion penetration at $i_{\text{cor}} = 10000 \mu\text{A}/\text{cm}^2$ and $i_{\text{cor}} = 0.1 \mu\text{A}/\text{cm}^2$ is less than 10 percent. For $t_0 = 10000$ days in Figure 9, the critical corrosion penetration increases monotonically with decreasing corrosion rate

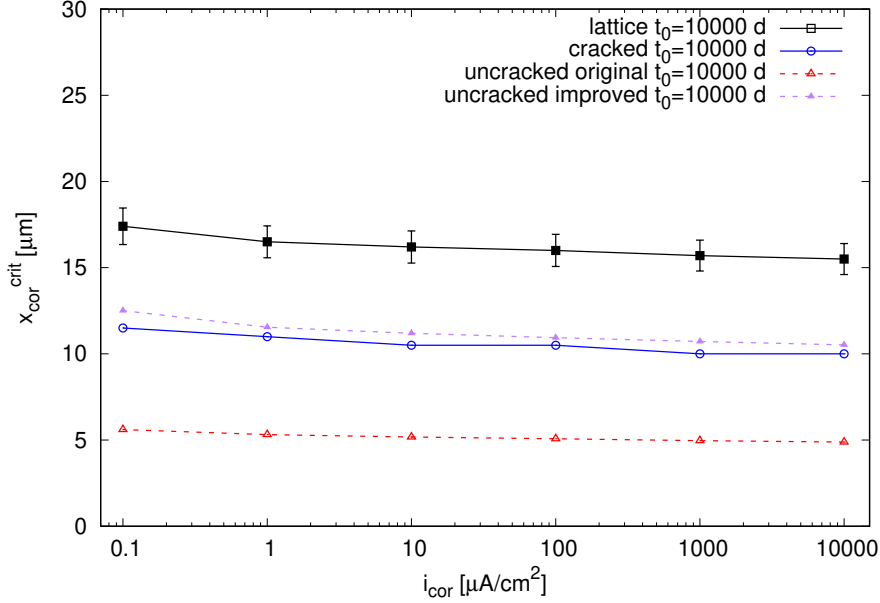


Figure 9: Critical penetration depth $x_{\text{cor}}^{\text{crit}}$ versus corrosion rate i_{cor} for loading at age $t_0 = 10000$ days.

for all three models. However, the increase of x_{cor} with increasing i_{cor} is much less pronounced than it was for $t_0 = 28$ days.

The trends in Figures 8 and 9 are the result of a number of factors, which are discussed here in more detail. Firstly, tensile strength evolves strongly with time. As concrete matures, tensile strength increases, as shown in Figure 10. The greater the tensile strength is, the more inner pressure the thick-walled cylinder can sustain, i.e., the greater is the critical corrosion penetration. The increase of tensile strength is much more pronounced for a loading at $t_0 = 28$ days than at $t_0 = 10000$ days. Therefore, for corrosion in mature concrete, changes in tensile strength are of minor importance. However, the change is important for laboratory tests for which corrosion commences soon after the concrete reaches its design strength and a small i_{cor} (long loading duration) is used. Concrete maturity at loading and load duration influence also the Young modulus of concrete. On the one hand, Young's modulus increases with age independently of the loading regime. On the other hand, concrete subjected to load undergoes creep, which decreases the effective modulus. In Figure 11, the effective modulus versus the load duration is shown for loading at $t_0 = 28$ and 10000 days. For the AAEM approach, the effective modulus is calculated from (13). For the lattice model, the effective modulus is determined from a single lattice element subjected to direct tension kept constant over time. By evaluating the secant modulus at increasing times, the evolution of the effective modulus is obtained. The values of the effective moduli for the lattice model were scaled so that the effective modulus for $t_0 = 28$ and $\Delta t = 0.01$ days is equal to the continuum Young's modulus E^{28} , which permits a direct comparison of the effective modulus and AAEM. For the AAEM approach used for the uncracked and cracked thick-walled cylinder model, the age-adjusted effective modulus $E''(t_0 = 28, \Delta t = 0.01)$ is equal to the target reference Young's modulus E^{28} . It can be seen that the maturity of concrete strongly affects the effective modulus. The increase in the effective modulus due to aging is stronger than the decrease due to creep. Furthermore, the younger the concrete is, the more the effective modulus decreases due to creep. Comparing AAEM

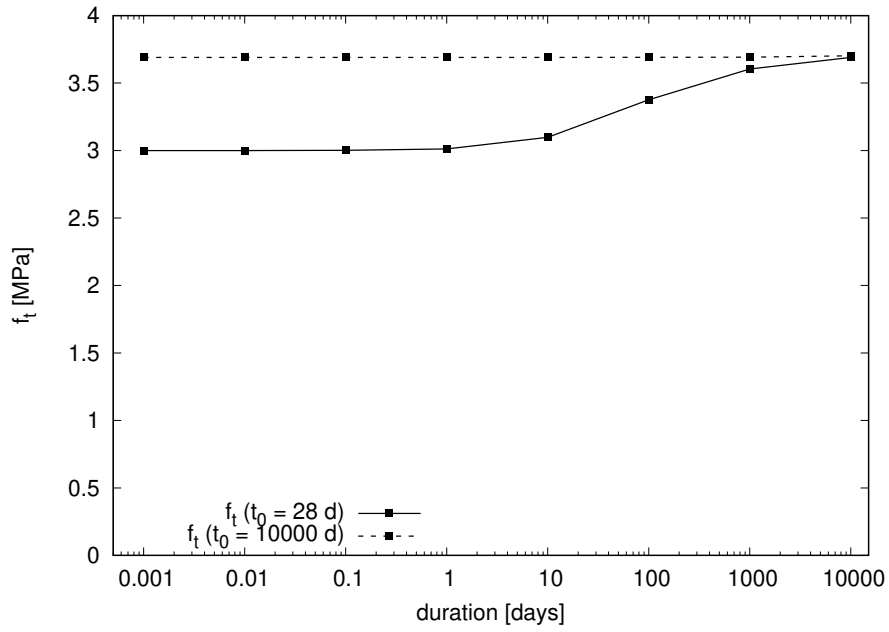


Figure 10: Tensile strength versus loading duration for loading at $t_0 = 28$ and 10000 days.

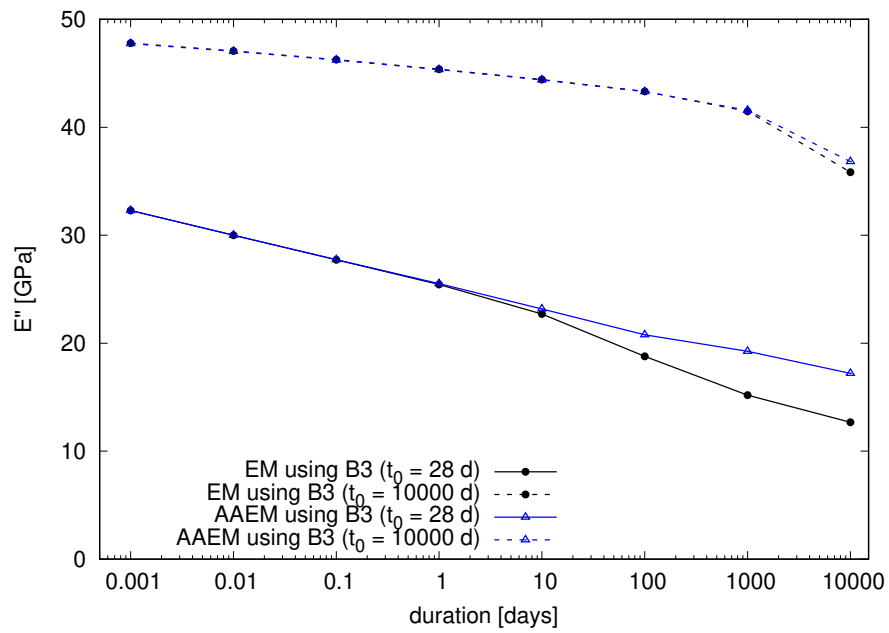


Figure 11: Effective modulus versus loading duration for start of loading at $t_0 = 28$ and 10000 days.

and EM, it is visible that the reduction of the effective modulus due to creep is stronger for the AAEM approach. This agrees with the trends presented in Bažant and Jirásek (2018).

The greater the effective modulus is, the smaller is $x_{\text{cor}}^{\text{crit}}$, because a stiffer material around the expanding layer of corrosion products will produce higher stresses. This effect is the most visible for the original version of the uncracked model in Figure 8, because in this model there is no reduction of stiffness due to cracking, whereas for the cracked and lattice model cracking is modelled, and the improved version of the uncracked model takes into account plastic strains. The critical corrosion penetration $x_{\text{cor}}^{\text{crit}}$ is the least affected by changes in the effective modulus in the lattice approach. In Figure 8, it is even visible that the critical corrosion penetration value decreases for corrosion current densities less than $10 \mu\text{A}/\text{cm}^2$ in the lattice model. This reversal in the trend of critical corrosion penetration can be explained by the competing influences of the evolution of tensile strength and Young's modulus. As explained above, aging of concrete increases the tensile strength and Young's modulus. An increase of tensile strength increases the critical corrosion penetration whereas an increase in Young's modulus results in a reduction of this penetration. The way in which these aging driven changes interact depends on the modelling approach.

4 Conclusions

Three modelling approaches of varying complexity have been used in this study of the effects of linear creep and aging of concrete on initiation of corrosion-induced surface cracking.

The overall conclusion from this study is that the more comprehensive the model is, the less important is the effect of linear creep and aging of concrete on corrosion-induced cracking. For corrosion starting at the age of 28 days, both creep and increase in strength and stiffness due to increasing maturity are very pronounced. However, the interaction of these competing processes results in critical corrosion penetrations which are not too sensitive to the corrosion rate. For corrosion in mature concrete, both creep and change in strength and stiffness are small. For the simpler models, particularly the uncracked model, the corrosion rate has a strong effect on the critical corrosion penetration for corrosion starting at $t_0 = 28$ days. This conclusion is important, since simpler mechanistic models use creep coefficients which produce critical corrosion penetrations that are very sensitive to the corrosion rate, as it was shown for the simpler models in the present study as well. Our finding with the comprehensive model shows that creep is not the source of sensitivity to corrosion rate. Instead, other variables should be introduced in predictive models which can explain the sensitivity of critical corrosion penetration to corrosion rate. Candidates for these variables would be the viscosity and expansion coefficient of corrosion products, as well as penetration of corrosion products into pores and cracks.

Other conclusions are that it has been shown that the three models predict the critical corrosion penetration very differently for fast corrosion rates, for which linear creep and aging have a small effect on the results. The uncracked model, which is the simplest of the three approaches, predicts in its original version the smallest critical corrosion penetration because it does not take into account the reduction of stiffness of the concrete due to cracking. The cracked model predicts greater critical corrosion penetrations because it models the cracking process. The improved version of the uncracked model accounts for plastic strains and provides an analytical upper bound to the pre-

dictions obtained with the cracked model. Finally, the lattice modelling approach usually predicts the greatest critical corrosion penetration (with the exception of very low corrosion rates applied at a young age) because it models also distributed cracking and nonlinearities in compression, which is not considered in the cracked model. These results are in agreement with the overall findings in the literature. The lattice model is, among the three approaches examined here, the only one which is general enough to consider nonuniform corrosion and more complex stress states.

Acknowledgements

Aldellaa is grateful for the financial support from the Ministry of Higher Education - Libya. Havlásek acknowledges the support of the Czech Science Foundation [grant GA ČR 19-20666S]. Jirásek acknowledges the support of the European Regional Development Fund (Center of Advanced Applied Sciences, project CZ.02.1.01/0.0/0.0/16_19/0000778). The lattice simulations were carried out with the finite element programme OOFEM (Patzák, 2012) modified by the authors.

References

- Alonso, C.; Andrade, C.; Rodriguez, J., and Diez, J. Factors controlling cracking of concrete affected by reinforcement corrosion. *Materials and Structures*, 31(7):435–441, 1998.
- Andrade, C.; Alonso, C., and Molina, F. J. Cover cracking as a function of bar corrosion: Part I-Experimental test. *Materials and Structures*, 26(8):453–464, 1993.
- Asahina, D.; Aoyagi, K.; Kim, K.; Birkholzer, J., and Bolander, J. E. Elastically-homogeneous lattice models of damage in geomaterials. *Computers and Geotechnics*, 81:195–206, 2017.
- Athanasiadis, I.; Wheeler, S. J., and Grassl, P. Hydro-mechanical network modelling of particulate composites. *International Journal of Solids and Structures*, 130–131:49–60, 2018.
- Balafas, I. and Burgoyne, C. J. Modeling the structural effects of rust in concrete cover. *Journal of Engineering Mechanics*, 137(3):175–185, 2011.
- Bažant, Z. P. and Jirásek, M. *Creep and hygrothermal effects in concrete structures*, volume 38. Springer, 2018.
- Bažant, Z. P. Prediction of concrete creep effects using age-adjusted effective modulus method. *ACI Journal*, 69:212–217, 1972.
- Bažant, Z. P. Physical model for steel corrosion in concrete sea structures: theory. *Journal of the Structural Division, ASCE*, 105(6):1137–1153, 1979a.
- Bažant, Z. P. Physical model for steel corrosion in concrete sea structures: application. *Journal of the Structural Division, ASCE*, 105(6):1154–1166, 1979b.
- Bažant, Z. P. and Baweja, S. Creep and shrinkage prediction model for analysis and design of concrete structures—model B3. Structural Engineering Report 94-10/603c, Northwestern University, 1994.

- Bažant, Z. P. and Baweja, S. Creep and shrinkage prediction model for analysis and design of concrete structures – model B3. *Materials and Structures*, 28:357–365, 1995. RILEM Recommendation, in collaboration with RILEM Committee TC 107-GCS, with Errata, Vol. 29 (March 1996), p. 126.
- Bhargav, K.; Ghosh, A. K.; Mori, Y., and Ramanujam, S. Model for cover cracking due to rebar corrosion in RC structures. *Engineering Structures*, 28(8):1093–1109, 2006.
- Bolander, J. E. and Saito, S. Fracture analysis using spring networks with random geometry. *Engineering Fracture Mechanics*, 61:569–591, 1998.
- Broomfield, J. P. *Corrosion of steel in concrete: understanding, investigation and repair*. Taylor & Francis, 1997.
- Bryant, A. H. and Vadhanavikkit, C. Creep, shrinkage-size, and age at loading effects. *ACI Materials Journal*, 84:117–123, 1987.
- Bushman, J. B. Calculation of corrosion rate from corrosion current (faraday’s law). *Bushman & Associates Inc*, 2000.
- Caballero, A.; Lopez, C., and Carol, I. 3d meso-structural analysis of concrete specimens under uniaxial tension. *Computer Methods in Applied Mechanics and Engineering*, 195(52):7182–7195, 2006.
- Chang, Ze; Zhang, Hongzhi; Schlangen, Erik, and Šavija, Branko. Lattice fracture model for concrete fracture revisited: Calibration and validation. *Applied Sciences*, 10(14):4822, 2020.
- Chernin, L.; Val, D. V., and Volokh, K. Y. Analytical modelling of concrete cover cracking caused by corrosion of reinforcement. *Materials and Structures*, 43(4):543–556, 2010.
- El Maaddawy, Tamer A and Soudki, Khaled A. Effectiveness of impressed current technique to simulate corrosion of steel reinforcement in concrete. *Journal of materials in civil engineering*, 15(1):41–47, 2003.
- Fahy, C.; Wheeler, S.; Gallipoli, D., and Grassl, P. Corrosion induced cracking modelled by a coupled transport-structural approach. *Cement and Concrete Research*, 94:24–35, 2017.
- Fédération Internationale du Béton, . *fib Model Code 2010*, 2012.
- Grassl, P. and Davies, T. Lattice modelling of corrosion induced cracking and bond in reinforced concrete. *Cement and Concrete Composites*, 33:918–924, 2011.
- Grassl, P. and Jirásek, M. Meso-scale approach to modelling the fracture process zone of concrete subjected to uniaxial tension. *International Journal of Solids and Structures*, 47:957–968, 2010.
- Grassl, P. and Rempling, R. Influence of volumetric-deviatoric coupling on crack prediction in concrete fracture tests. *Engineering Fracture Mechanics*, 74:1683–1693, 2007.
- Grassl, Peter; Jirásek, Milan, and Gallipoli, Domenico. Initiation of fluid-induced fracture in a thick-walled hollow permeable sphere. *European Journal of Mechanics-A/Solids*, 76:123–134, 2019.

- Jamali, A.; Angst, U.; Adey, B., and Elsener, B. Modeling of corrosion-induced concrete cover cracking: A critical analysis. *Construction and Building Materials*, 42:225–237, 2013.
- Jirásek, M. and Grassl, P. Evaluation of directional mesh bias in concrete fracture simulations using continuum damage models. *Engineering Fracture Mechanics*, 75(8):1921–1943, 2008.
- Jirásek, M. and Havlásek, P. Microprestress–solidification theory of concrete creep: Reformulation and improvement. *Cement and Concrete Research*, 60:51–62, 2014.
- Jirásek, M. and Havlásek, P. Accurate approximations of concrete creep compliance functions based on continuous retardation spectra. *Computers and Structures*, 135:155–168, 2014.
- Kommendant, G.J.; Polivka, M., and Pirtz, D. Study of concrete properties for prestressed concrete reactor vessels, final report - part II, creep and strength characteristics of concrete at elevated temperatures, rep. no. ucseem 76-3 prepared for general atomic company. Technical report, Dept. Civil Engineering, Univ. of California, Berkeley, 1976.
- L’Hermite, R.; Mamillan, M., and Lefèvre, C. Nouveaux résultats de recherches sur la déformation et la rupture du béton. *Supplément aux Annales de L’Institut Technique du Bâtiment et des Travaux Publics*, 207/208:325–345, 1965.
- Li, C.-Q.; Melchers, R. E., and Zheng, J.-J. Analytical model for corrosion-induced crack width in reinforced concrete structures. *ACI Structural Journal*, 103(4):479–487, 2006.
- Liang, Yongqin and Wang, Licheng. Prediction of corrosion-induced cracking of concrete cover: A critical review for thick-walled cylinder models. *Ocean Engineering*, 213:107688, 2020.
- Liu, Y. and Weyers, R. Modeling the time-to-corrosion cracking in chloride contaminated reinforced concrete structures. *ACI Materials Journal*, 95(6):675–680, 1998.
- Lundgren, Karin. Bond between ribbed bars and concrete. Part 2: The effect of corrosion. *Magazine of Concrete Research*, 57(7):383–395, 2005.
- Michel, A.; Pease, B. J.; Peterová, A.; Geiker, M. R.; Stang, H., and Thybo, A. E. A. Penetration of corrosion products and corrosion-induced cracking in reinforced cementitious materials: Experimental investigations and numerical simulations. *Cement and Concrete Composites*, 47: 75–86, 2014.
- Molina, F.; Alonso, C., and Andrade, C. Cover cracking as a function of rebar corrosion: Part II-numerical model. *Materials and Structures*, 26(9):532–548, 1993.
- Montero-Chacón, F.; Cifuentes, H., and Medina, F. Mesoscale characterization of fracture properties of steel fiber-reinforced concrete using a lattice–particle model. *Materials*, 10(2):207, 2017.
- Mullard, J. A. and Stewart, M. G. Corrosion-induced cover cracking of RC structures: new experimental data and predictive models. Technical report, University of Newcastle, 2009.
- Ouglova, A.; Berthaud, Y.; François, M., and Foct, F. Mechanical properties of an iron oxide formed by corrosion in reinforced concrete structures. *Corrosion Science*, 48:3988–4000, 2006.
- Pantazopoulou, S. J. and Papoulia, K. D. Modeling cover-cracking due to reinforcement corrosion in RC structures. *Journal of Engineering Mechanics*, 127(4):342–351, 2001.

- Patzák, B. OOFEM – An object-oriented simulation tool for advanced modeling of materials and structure. *Acta Polytechnica*, 52:59–66, 2012.
- Pedrosa, F. and Andrade, C. Corrosion induced cracking: Effect of different corrosion rates on crack width evolution. *Construction and Building Materials*, 133:525–533, 2017.
- Robuschi, S.; Tengattini, A.; Dijkstra, J.; Fernandez, I., and Lundgren, K. A closer look at corrosion of steel reinforcement bars in concrete using 3D neutron and X-ray computed tomography. *Cement and Concrete Research*, 144:106439, 2021.
- Roshan, Arman; Noël, Martin, and Martín-Pérez, Beatriz. Validation of thick-walled cylinder analogy for modelling corrosion-induced concrete cover cracking. *Construction and Building Materials*, 238:117724, 2020.
- Schlangen, E. and van Mier, J. G. M. Simple lattice model for numerical simulation of fracture of concrete materials and structures. *Materials and Structures*, 25:534–542, 1992.
- Tepfers, R. Cracking of concrete cover along anchored deformed reinforcing bars. *Magazine of Concrete Research*, 31(106):3–12, 1979.
- Thilakarathna, P. S. M.; Kristombu Baduge, K. S.; Mendis, P.; Vimonsatit, V., and Lee, H. Mesoscale modelling of concrete—a review of geometry generation, placing algorithms, constitutive relations and applications. *Engineering Fracture Mechanics*, 231:106974, 2020.
- Wong, H. S.; Zhao, Y. X.; Karimi, A. R.; Buenfeld, N. R., and Jin, W. L. On the penetration of corrosion products from reinforcing steel into concrete due to chloride-induced corrosion. *Corrosion Science*, 52:2469–2480, 2010.
- Yip, M.; Mohle, J., and Bolander, J. E. Automated Modeling of Three-Dimensional Structural Components Using Irregular Lattices. *Computer-Aided Civil and Infrastructure Engineering*, 20(6):393–407, 2005.
- Zhao, Y.; Karimi, A. R.; Wong, H. S.; Hu, B.; Buenfeld, N., and Jin, W. Comparison of uniform and non-uniform corrosion induced damage in reinforced concrete based on a gaussian description of the corrosion layer. *Corrosion Science*, 53(9):2803–2814, 2011.
- Zhou, R. and Lu, Y. A mesoscale interface approach to modelling fractures in concrete for material investigation. *Construction and Building Materials*, 165:608–620, 2018.